

Cite this: DOI: 00.0000/xxxxxxxxxx

Evolution of Adaptive Force Chains in Reconfigurable Granular Metamaterials[†]

Sven Witthaus,^a Atoosa Parsa,^b Nidhi Pashine,^a Jerry Zhang,^a Arthur Mackeith ^a, Mark D. Shattuck^c, Josh Bongard,^b Corey S. O'Hern,^{a,d} and Rebecca Kramer-Bottiglio^a

Received Date
Accepted Date

DOI: 00.0000/xxxxxxxxxx

Under an externally applied load, granular packings form force chain networks that depend on, among other things, the contact network and stiffness of the grains. In this work, we investigate packings of variable stiffness particles, where we can direct the force chains by changing the stiffness of individual particles within the packing on demand. Each variable stiffness particle is made of a silicone shell that encapsulates a core made of a low-melting point metallic alloy (Field's metal). By sending an electric current through a co-located copper heater, the Field's metal internal to each particle can be melted via Joule heating, which causes softening of the particle. As the particle cools to room temperature, the alloy solidifies and the particle recovers its original stiffness. To optimize the mechanical response of granular packings containing both soft and stiff particles, we employ an evolutionary algorithm coupled with a discrete element method simulation to predict the stiffness patterns that will yield a particular force output on the assembly boundary. The predicted stiffness patterns were built in experiments using a 2D assembly of variable stiffness particles and the force outputs at different points of the assembly boundary were measured using photoelasticity. This result is a first step towards making robotic granular metamaterials that can dynamically adapt their mechanical properties such as force transmission, elastic moduli, and frequency response on demand.

1 INTRODUCTION

Mechanical metamaterials exploit mechanical inputs, such as forces, pressures, or waves, to achieve programmable shape transformations, force propagation, and stiffness¹⁻³. Many current mechanical metamaterial approaches focus on continuum solids or linkages/mechanisms with a fixed structure and therefore demonstrate only fixed responses. We are interested in mechanical metamaterials that can exhibit increased dynamic plasticity, enabling adaptation to different environmental inputs or task demands by reconfiguring their physical structure. Granular metamaterials—consisting of discrete particles—offer an advantageous platform for such dynamic programmability, as individual particle properties can be tuned to achieve different bulk responses⁴. As an example, one can imagine a granular metamaterial that uses individual particle adaptations to route forces

around a shielded part of the material so that it can maintain function after damage (Fig. 1).

Many groups have developed granular metamaterials using grains that are enclosed within stretchable elastic skins and connected to a vacuum source⁵⁻⁸ or shear⁹⁻¹¹ to induce jamming transitions in these materials. When unjammed, the bulk material is compliant, and when jammed, the bulk material can achieve the stiffness of the hard grains. Prior studies have produced changes in stiffness between the compliant and jammed states on the order of 50×, and this jamming technology has been applied to soft robotics¹²⁻¹⁶, surgical devices^{17,18}, flexible airfoils¹⁹, and programmable aggregate architecture²⁰. However, granular metamaterials most often incorporate ordered assemblies, as it is much more difficult to predict the material properties of disordered granular assemblies. Ordered granular metamaterials have been used for vibration mitigation²¹⁻²⁵, acoustic switches^{26,27}, energy absorption²⁸, modulus and density tuning^{29,30}, and non-reciprocal behaviors³¹. Most of these prior studies have confined their approach to granular systems with inert, rigid grains. Herein, we attempt to expand the dimensionality of the parameter space by including variable stiffness particles, thereby enabling access to a wider set of possible material responses.

We previously developed Discrete Element Method (DEM) sim-

^a Department of Mechanical Engineering and Materials Science, School of Engineering and Applied Science, Yale University, 9 Hillhouse Ave., New Haven, CT 06511, USA. E-mail: rebecca.kramer@yale.edu

^b Department of Computer Science, University of Vermont, Innovation 428, Burlington, VT 05405, USA

^c Benjamin Levich Institute and Physics Department, The City College of the City University of New York, NY, New York 10031, USA

^d Department of Physics, Yale University, New Haven, CT 06520, USA

[†] Electronic Supplementary Information (ESI) available. See DOI: 00.0000/00000000.

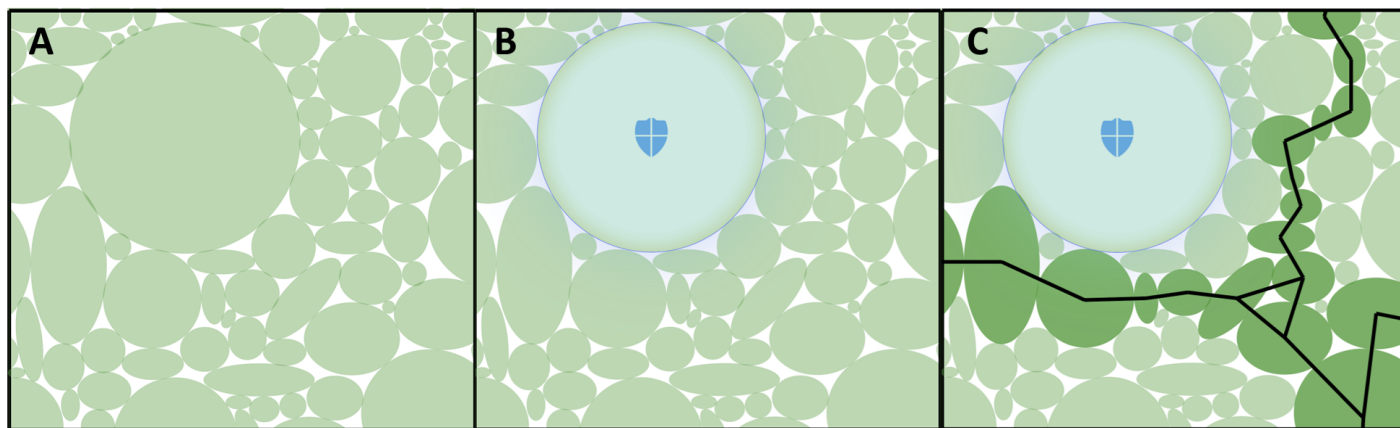


Fig. 1 Schematic of a granular packing made of variable stiffness (VS) particles. (Left) An original jammed granular packing. (Middle) We wish to shield a particle in the middle of the packing from any forces. A damaged particle might need to be shielded if it cannot withstand loads. (Right) By changing the stiffness of some particles, we can redirect the force network to avoid the shielded area, allowing the system to withstand loads. Soft and stiff particles are depicted in light and dark green, respectively.

ulations to study the vibrational response of jammed packings composed of binary mixtures of spherical particles of the same size, but different masses. In a recent study²⁷, we showed that 2D and 3D granular assemblies can be used to either transmit or block vibrations with particular frequencies, thereby creating a mechanical transistor. Expanding upon that result, we then applied Evolutionary Algorithms (EA) to the DEM simulation to create more complex logic gates^{32–34}. Using the same granular system, in this work we study the transmission of force chains. By switching the stiffness of individual particles, we achieve dynamic modification of the force distribution through a packing in both simulation and reality.

In general, granular packings are a collection of macroscopic particles that are densely packed together forming a contact network through which forces are distributed. In frictionless packings, each grain exerts normal forces at its contacts to prevent the packing from collapsing. Though the contact network is known to be easily perturbed by applying a large external load^{35–39}, a large fraction of the load is often carried by a small fraction of particles, resulting in the emergence of stable force chains⁴⁰. Due to the large number of variables present in a granular system, force chain dynamics are challenging to study analytically and therefore have been studied through contact dynamics simulations⁴¹, DEM^{42,43}, and models based on statistical mechanics⁴⁴. Though the unpredictable nature of the force chains is largely a function of the disordered contact network, individual particle properties, such as stiffness or density, are known to influence how forces propagate through the assembly⁴⁵.

Our instantiation of a granular metamaterial with adaptable force chains is realized through an assembly of variable stiffness (VS) particles. While there are many potential approaches to particle stiffness modulation, we adapt the approach previously used by Pashine *et al.*⁴⁶ to make variable stiffness bonds in an allosteric metamaterial. Our VS particles are fabricated by incorporating Field’s metal cores in soft silicone shells. Field’s metal is an alloy of indium, bismuth, and tin with a low melting point of 62 °C. While solid, Field’s metal has a Young’s modulus of 9.25 GPa⁴⁷,

which reduces to almost zero at the melting temperature (limited by the incompressibility of the liquid). Correspondingly, a VS particle possesses a high stiffness when the Field’s metal core is solid and a low stiffness when the core is liquid. Using DEM simulations combined with evolutionary algorithms, we identify configurations that optimize specific force outputs on the assembly boundary. We then construct these configurations into experiment and show that we can switch the stiffness of individual particles to adapt the packing’s force chain networks on demand. Finally, we augment our multi-objective optimization to prioritize power efficiency with the assumption that 1) the particles consume power when softened, as is the case in our present instantiation, or 2) the particles consume power when switching stiffness, which may be the case in a different instantiation. In all cases, our simulation-to-reality gap is relatively small. Overall, this work represents an important step towards dynamic granular metamaterials that can adapt their properties in response to changing environments or task demands.

2 Methods

To controllably modify the force network of a packing, we created a pipeline that takes a set of objectives (e.g., maximize the forces on specific particles) and hardware constraints as inputs, and outputs the configuration of low/high stiffness particles corresponding to the objective. Our pipeline has several preamble steps. First, we must have physical VS particles to characterize their relevant contact mechanics and corresponding interparticle force law. Second, we embed the measured particle physics into our DEM particle simulator, such that the simulator is as representative as possible of the physical hardware. With an accurate simulator in place, we can then begin to define objectives and employ a multi-objective optimization to design candidate particle assembly designs, as shown in Fig. 2.

The inverse design problem—designing particle configurations to match a desired force chain output—would be an arduous manual task. Without a systematic way of arriving at a certain force network, we would have to evaluate an exponentially large

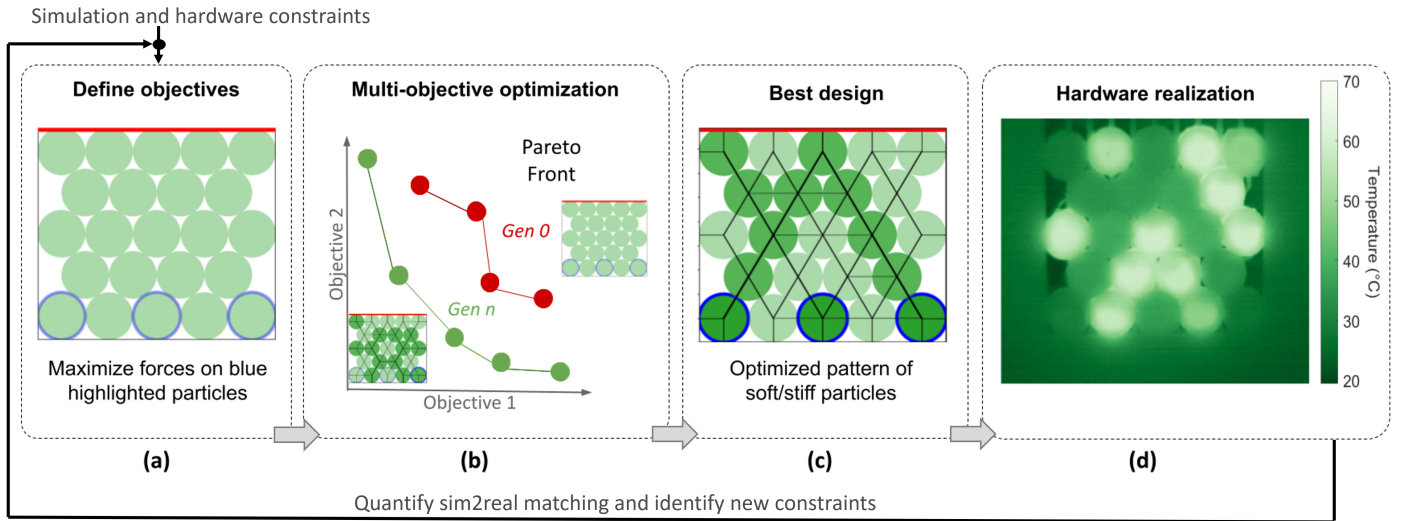


Fig. 2 Simulation to reality (sim2real) pipeline description. (a) We start with a simulation that has been tuned to match our hardware (VS particle) data. We then define optimization objectives for our packing alongside hardware constraints. (b) Using multi-objective optimization, we can find the packing that best satisfies our objectives. The algorithm starts with a set of randomly generated configurations in the first generation (Gen 0). During the optimization process, configurations that better satisfy the objective(s) are replaced in the solution set (Gen n). (c). We can realize this packing in hardware (d) and use the outcome to define additional hardware constraints that will improve the match between simulations and experiments.

number of configurations to decide which configuration is closest to the desired network. Finding analytical solutions for arbitrarily complicated packings is unfeasible and therefore much more suited to be done in simulations. Thus, we use a multi-objective optimization algorithm to search for solutions that satisfy our objectives as well as respect any hardware constraints set by the limitations of our experiments. We can then make the materials obtained from our optimization pipeline and evaluate their force networks, ensuring that the objectives have been met. By comparing the results obtained in experiments to the results from simulations, we can identify important missing properties in our simulation, thereby closing the loop.

2.1 Experimental Design

In the sections below, we describe the design and fabrication of the VS particles and how force networks are evaluated in VS particle packings.

2.1.1 Variable Stiffness Particles

We make the variable stiffness (VS) particles using Field’s metal, an alloy of bismuth, indium, and tin with a melting temperature of 62° . We encapsulate a solid cylinder of Field’s metal inside a soft silicone shell made from Smooth-on Dragonskin™ 10 (Figure 3A). We place a small copper heater inside the shell that allows us to melt the Field’s metal via Joule heating. The high-resistance copper heater is separated from the Field’s metal by a thin layer of silicone to avoid shorting the heater. By running current (≈ 1 A) through the heater we can melt the Field’s metal inside, thereby inducing a substantial change in stiffness.

Next, we measure the interparticle interactions between our VS particles. Consider two VS particles placed in contact with their axes parallel to each other. The interparticle force law for two cylindrical particles with Hertzian interactions is described by⁴⁸:

$$d = \bar{F}(V) \left(1 + \ln \left(\frac{4L^2}{V\bar{F}D} \right) \right) \quad (1)$$

where d is the total deformation of the particles, \bar{F} is the normal force per unit length between the particles, and $V = \frac{2(1-\nu^2)}{\pi E}$, a common measure of the modulus of a two-particle system. Therein, E is the Young’s Modulus of the material, ν is the Poisson’s ratio of the material, D is the diameter of the particles, and L is the length of the particles (cylinders).

We obtain the value of V in the above equation by compressing single VS particles between two steel surfaces using a material testing system (Instron) and fitting the resulting force-displacement curve to equation 1 (Figure 3B). The VS particles are much softer than the steel surface we compress them on ($V_{steel} \ll V_{particles}$). Thus, we can plot the particle compressive modulus ($= \frac{2}{\pi V} = \frac{E}{1-\nu^2}$) against temperature to show the stiffness phase transition obtained at temperatures higher than $T > 62^\circ\text{C}$.

2.1.2 Particle Assembly

We assemble the VS particles in a triangular lattice where each particle can be actuated (heated) individually using a micro-controller (Arduino™). However, heat from actuated particles eventually dissipates into the neighboring non-actuated particles, causing thermal crosstalk. To mitigate thermal crosstalk, we established limits on the actuation power of each VS particle (see ESI† S1).

We apply a uniform load to the top layer of particles using the same materials testing system used to characterize the VS particles. The force propagates through the packing to create a particular force network that is a function of the positions of the particles and their individual stiffnesses. Based on the location of the stiff and soft particles, the force travels differently to the bottom row of particles, exerting different amounts of force at different

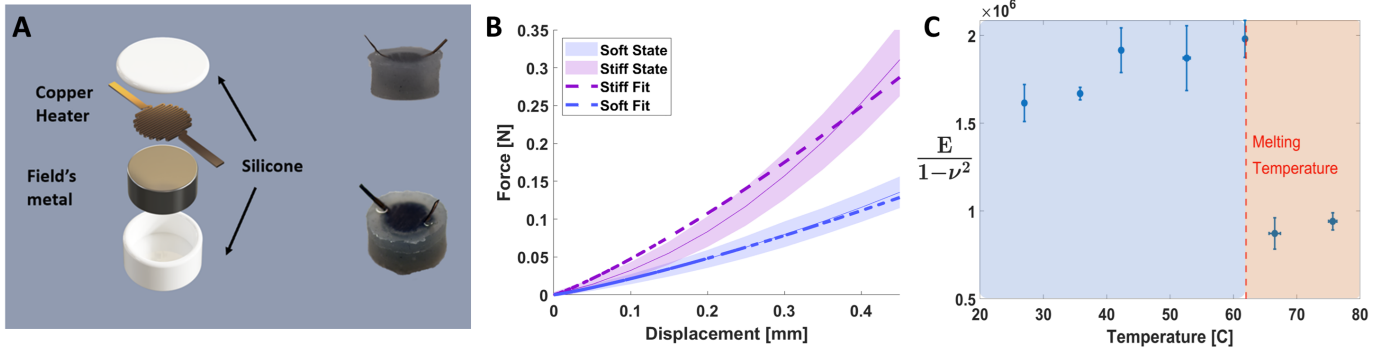


Fig. 3 Variable stiffness (VS) particle characterization. (A) Rendering of a VS particle next to its real counterpart. (B) Force-displacement plot for VS particles in their soft and stiff states, with Hertzian fits plotted as dashed lines. (C) Modulus $\frac{E}{1-\nu^2}$ plotted as a function of temperature. The particle modulus decreases above the melting temperature of Field's metal. The compressive modulus in its heated (soft) state is approximately $2.5\times$ smaller than in the cooled (stiff) state.

locations on the assembly boundary.

The assembly boundary (or wall) is made of a photoelastic material (ClearFlex™ 95) placed between two circular-crossed polarizers. We measure the output forces on the boundary by analyzing the stress-induced birefringence^{39,49,50}. When the boundary is under no stress, no light passes through the polarizers. Any stress on the boundary rotates the direction of the incoming electric field, allowing it to pass through the polarizer and visually present as a fringe pattern. Because different wavelengths of light will form different patterns at the photoelastic wall, we use a filter to only observe one wavelength of light (530 nm).

To measure the forces on the boundary, we consider the intensity image that will be formed by the application of a point force on an elastic half-space through a polariscope^{51,52}:

$$I_{out} = I_0^2 \sin^2 \frac{\pi t K}{\lambda} (\sigma_1 - \sigma_2), \quad (2)$$

where t is the thickness of the material, K is the material-dependent stress-optic coefficient, λ is the wavelength of light used, and $\sigma_1 - \sigma_2$ is the principle stress difference, which in our system corresponds to the normal stress measured radially outward from the particle-wall contact. Therefore,

$$\sigma_1 - \sigma_2 = \left| \frac{2}{\pi r} F (\cos \phi \sin \theta + \sin \phi \cos \theta) \right|, \quad (3)$$

where r and θ denote the distance from the point force and the angle to the x-axis, respectively, F is the total applied force per unit length, and ϕ determines the angle of the force in the normal and tangential directions.

Using Equations 2 and 3, we can construct an image for a given input force on a half-plane. By comparing this image to our experimentally obtained image, we can fit our force using minimum chi-square least square estimation⁵¹. We note that it is difficult to extract an exact value for K , and we instead fit our curve to the factor $2tKF$, which results in a measure of F up to a normalization constant (see ESI† S2).

2.2 DEM simulations

We employ a discrete element method (DEM) simulation that mimics the physical setup used in the experiment. A collection of

two-dimensional, monodisperse, and frictionless particles is assembled in a triangular lattice. We apply a constant force from the top boundary onto the packing. Each particle interacts with its neighbors and the wall, assuming a purely repulsive potential with a Hertzian pressure distribution, as in Equation 1. We update each particle's position using modified velocity Verlet integration scheme assuming a constant damping coefficient and end the simulation once the net force on all particles $< 10^{-10}$ N. Noting which of our disks are in contact allows us to construct the network of inter-particle contacts, as shown in Figure 2c.

There are differences between simulation and experiment. For example, the simulation does not account for substrate and interparticle friction. We mitigate these effects by applying a thin layer of cornstarch over each of the variable stiffness particles in the physical experiment, thus decreasing the effective friction in our system. Still, slight inconsistencies between the particle sizes lead to polydispersity in the experiment, while the simulation assumes monodispersity. Further discrepancies between the real and simulated particle deformations will contribute to imperfect matching between simulation and reality.

2.3 Optimization Setup

Evolutionary Algorithms (EAs) are a class of population-based gradient-free optimization methods that are inspired by natural evolution. The algorithm starts with a population of randomly generated solutions. At each subsequent step, until reaching the stopping criteria, the fittest solutions are chosen to reproduce and survive to the next generation. EAs have been useful in a myriad of problems in materials science⁵³, robotics⁵⁴, and more practical, scheduling and data retrieval applications⁵⁵. In this work, we used EAs to find an optimal configuration of soft and stiff particles to reach a desired contact network or force output on the particle assembly boundary.

The EA has multiple components including genome representation, variation operators, and fitness function. We used a direct encoding scheme for the genome, where the genotype is a binary string representing the placement of soft and stiff particles on a triangular grid. Since our objective is to maximize the amount of force specific particles exert on the bottom assembly wall, we

use the force as the fitness value when evaluating a configuration during the evolutionary optimization process.

3 Results

3.1 Feasibility check: maximizing force on a single particle

To verify that the simulation uses the appropriate force law and that the EA generates reasonable solutions, we initially choose a simple problem with a predictable outcome. We searched for the optimal configuration of soft/stiff particles that takes a uniform input force on the top row of particles and maximizes the output force by the middle particle in the bottom row on the bottom wall (Fig. 4A).

During the optimization, each candidate solution is evaluated by measuring the force the bottom middle particle applies on the bottom wall at a constant input force of 1 (arbitrary units). Using Age-Fitness Pareto Optimization (AFPO)⁵⁶ we can find a configuration of particles where this objective is maximized. AFPO was developed to solve the premature convergence problem where the algorithm fails to make any progress after converging to a local optimum. The algorithm works by tracking the age of each individual in the population and allowing the newly added individuals to survive to the next generation before being dominated by the more fitted solutions. At the last generation of the optimization, the algorithm converges to a set of non-dominated Pareto optimal solutions. AFPO was run with a population size of 50 for 250 generations and a total of 3 independent trials were performed each starting with a population of randomly generated solutions. To achieve more variation across populations, we implement a bit-flip mutation that randomly switches the stiffness of a grain with a probability of 0.05 (no cross-over operator was implemented). As we can see in Fig. 4B, the best configuration emerges after only 100 generations. In the histogram plotted along the y-axis, we find that the best solution found by EA outperforms the result of a random search with 5000 configurations.

As shown in Fig. 4C, the resulting configuration contains two lines of stiff particles that stretch from the top wall to the bottom wall. This solution is intuitive, as higher forces will be carried by stiffer particles. Thus, arranging stiff particles such that they form a path from the input to the output will result in a large force carried to the bottom particle.

To validate the result obtained by the EA, we recreate the pattern of particles in experiments and characterize the output force on the wall as a function of the input force. Additionally, we make two randomly generated patterns in experiments and compare the force outputs to the best-performing solution (Fig. 4D). We can take the slope of the output vs. input force curve to be our normalized force output. We can obtain the same metric in simulation by dividing our output by the input force. This gives us a unitless number to use as comparison between different configurations in both experiments and simulations. As shown in Fig. 4E, the best-performing configuration significantly outperforms the two random configurations.

We observe differences between the simulated and real force output results: The experiment force output is higher than the predicted force output in DEM simulation. This difference be-

tween simulation and experiment could be due to a variety of possible factors. Our particles are a composite of two materials that have a complicated non-linear elastic behavior which, in the simulation, is approximated to a Hertzian force response. Additionally, our DEM simulations does not include important factors such as substrate friction, polydispersity, or particle deformation. These factors lead to quantitative differences between the simulations and experimental force values. Despite these quantitative differences, we observe that the force outputs between the experiment and simulation are in qualitative agreement. A more careful matching between simulations and experiments might give insight into the relevance of each of these factors, which we hope to understand in detail in future studies.

3.2 Complex cases: maximizing forces on multiple particles

Having confirmed the accuracy of the simulation and the predictive ability of the EA, we apply the pipeline to objectives with non-intuitive solutions. Furthermore, using our individually addressable VS particles, we can search for pairs of solutions. That is, to adapt the packing from one distribution of forces to another, we can adapt the individual particle stiffnesses. To do the same with inert particles, one would need to create a packing in one configuration, then undo it and create a new packing in a second configuration. With our VS particles, we can change the contact network without deconstructing the packing.

To test the efficacy of our optimization pipeline towards a solution pair, we first define the two objective configurations:

- Configuration 1 (C_1) is better than random at maximizing the forces applied by the odd particles on the bottom wall.
- Configuration 2 (C_2) is better than random at maximizing the forces applied by the even particles on the bottom wall.

For each of these configurations, we assign an appropriate algorithmic objective. To find configuration C_1 , we want to maximize $O_1 = F_1 F_3 F_5$, where F_i stands for the force the i -th particle exerts on the bottom wall (counting from left to right). Similarly, to find C_2 we wish to maximize $O_2 = F_2 F_4$.

3.2.1 Optimal solutions with two objectives

To solve the multi-objective optimization problem of maximizing forces in configurations $\{C_1, C_2\}$, we use a popular and powerful EA called Non-dominated Sorting Genetic Algorithm II (NSGA-II)⁵⁷. Here, each solution consists of two configurations, each with 23 particles, that are either soft or stiff. The parameter space of each solution, or the genotype is a binary string of length 46 that contains the stiffness information of our two configurations. Our variation operator applies bit-flip mutation with probability 0.8 or one-point cross-over with probability 0.2.

The solutions in the Pareto front set at the end of the optimization loop are shown in Fig. 5A. We refer to these solutions as C_1^0 and C_2^0 . For the solution that maximizes the force applied by the odd particles, C_1^0 , we find lines of stiff particles going from the force input on the top row of particles to the output sites, reminiscent of the type of pattern that formed in our prior example. Similarly, for the solution that maximizes the force applied by the

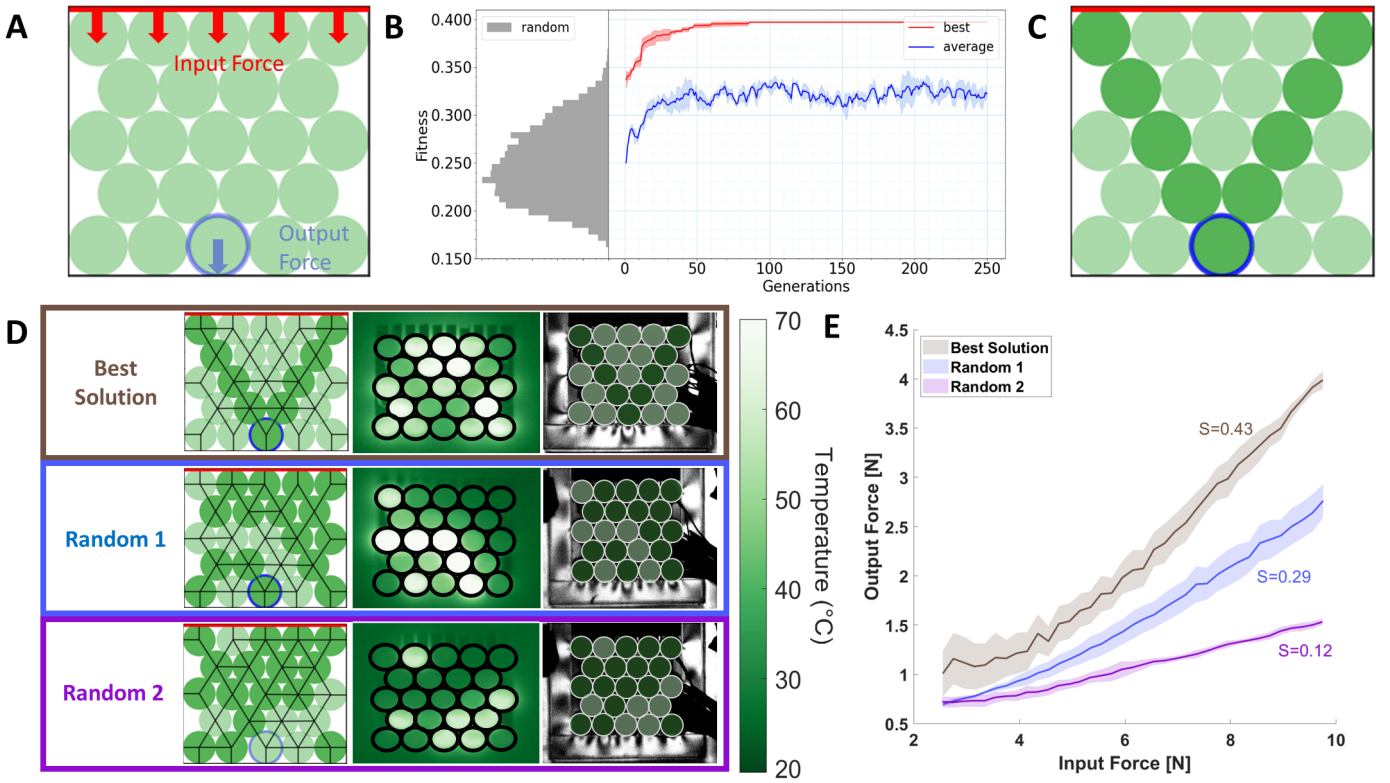


Fig. 4 Optimization assessment. (A) Schematic of the defined objective: maximize the force output from the middle particle in the bottom row given a uniform force input onto the top row. (B) Fitness of the best solution found and the average fitness of the whole population, as a function of evolution time (number of generations). Results are averaged over three independent trials. The result of the evolutionary algorithm outperforms a random search of over 5000 configurations (left). (C) The best solution found by the evolutionary algorithm. Soft and stiff particles are plotted in light and dark green, respectively. (D) Experimental realization: The first column shows three configurations with the predicted contact network in simulation. The second column shows thermal images of the experimental packing. The third column shows the fringe patterns formed on the photoelastic boundary. The three rows represent three different configurations. (E) Output force on the bottom wall under the middle particle as a function of input force on the top row of particles, for each of the configurations shown in (D). Error clouds represent ± 1 standard deviation across three trials. The slope (S) of a linear fit is written adjacent to the curves.

even particles, C_2^0 , we observe that the assembly side walls reflect the force back into the packing. We can switch between these two configurations using our VS particles.

We then translated C_1^0 and C_2^0 into physical experiments. By least-squares fitting of the photo-elastic pattern on the bottom boundary of the assembly, we find the resulting force distribution for a given input force on the top wall. Similar to Figure 4E, we take the input force versus output force for each of the particles on the bottom boundary. In Figure 5B, we plot the slope of that curve as our normalized force measurement for all the bottom particles.

The plots in Figure 5B show the predicted normalized force by each particle on the bottom boundary in simulations, as well as the corresponding experimental measurements. We find that the resulting force distribution is very similar to the distribution predicted by our simulations. Odd particles in C_1^0 and even particles in C_2^0 have a higher force output than the other particles on the bottom boundary. While we observe a high level of agreement between experiment and simulation, the output forces in experiments (O_1^0 and O_2^0) are higher than those predicted by the simulation. A continuous transition from packing C_1^0 to C_2^0 can be found in Movie S1 (ESI †).

3.2.2 Optimal solutions with three objectives

3.2.2.1 Minimizing soft particles. Our VS particle instantiation consumes energy to soften and remain softened. That is, the co-located heater must keep the embedded FM above its melting temperature for a particle to exhibit softening. Therefore, we exercised our optimization pipeline using the same two configurations and objectives $\{C_1, C_2; O_1, O_2\}$ with an added objective: we aim to minimize the total number of soft particles. We formalize this third objective as: $O_3 = (1 + N_{C_1}) \times (1 + N_{C_2})$, where N_{C_1} and N_{C_2} are the number of soft particles in configurations C_1 and C_2 , respectively. Minimizing the total number of soft particles in either configuration corresponds to a minimized energy expenditure, while still fulfilling O_1 and O_2 .

We ran the optimization using NSGA-II with a population size of 100 for 800 generation in 5 independent trials. The algorithm converged to a set of non-dominated Pareto optimal solutions. The best solution was selected by ranking the Pareto-optimal solutions using the Technique for Order of Preference by Similarity to Ideal Solution (TOPSIS) method⁵⁸.

For the first configuration (C_1), we find the best solution that maximizes $\{O_1, O_2\}$ and minimizes O_3 , is the same as the solution

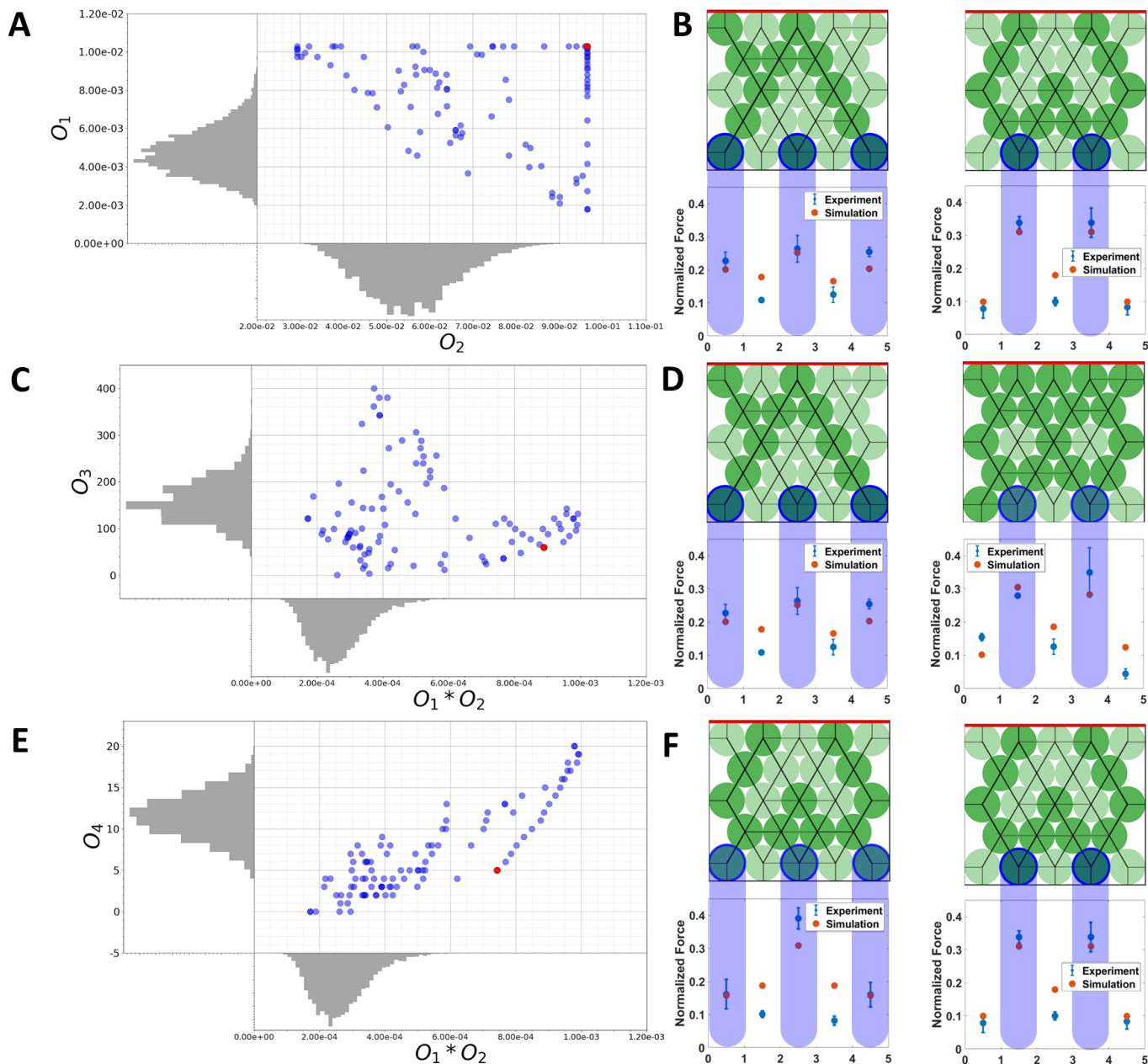


Fig. 5 Multi-objective optimization assessment. (A) A two-objective optimization. Solution sets were evolved to maximize forces on the odd particles (O_1) and even particles (O_2) in the bottom row. Pareto Front of the last generation of the evolutionary algorithm is plotted with random searches plotted adjacent to their axes. (B) The solution plotted in red is shown schematically on the right and defined as $\{C_1^0, C_2^0\}$. Underneath the $\{C_1^0, C_2^0\}$ schematics are the corresponding normalized force measurements from the experiment (blue) and simulation (orange). (C, D) Maximizing O_1 and O_2 , while minimizing O_3 , which is the number of particles that switch stiffness between configurations 1 and 2. The two-dimensional Pareto Front is shown by plotting O_3 versus O_1O_2 . (E, F) Maximizing O_1 and O_2 , while minimizing O_4 , which is the number of soft particles in configurations 1 and 2. The two-dimensional Pareto Front is shown by plotting O_4 versus O_1O_2

that only maximizes $\{O_1, O_2\}$ (C_1^0). The second configuration, (C_2) has many fewer soft particles compared to C_2^0 (Figure 5B). This result indicates an algorithmic preference for minimizing the number of soft particles in the second configuration. We visualize the resulting Pareto Front in two dimensions by plotting O_3 vs the product $O_1 \times O_2$. Although all solutions in the Pareto Front have gone through the selection process and are therefore optimized, we pick the configurations with the desired trade-off between the

multiple objectives to translate to experiments using TOPSIS.

3.2.2.2 Minimizing particle stiffness switches. With a different VS particle instantiation, it could be that energy is consumed to switch the stiffness of the particle, but not to hold it in either a softened or stiffened state. In that case, energy minimization would be the distance between two configurations in the solution space. We therefore introduce a corresponding objective: we aim to minimize the number of particles that switch

stiffness between C_1 and C_2 . Formally, this fourth objective is defined as: $O_4 = N_{C_1 \rightarrow C_2}$, which is the number of particles that switch stiffness between the configurations. We then re-engage our multi-objective optimization while maximizing $\{O_1, O_2\}$ and minimizing O_4 .

The Pareto front is shown for O_4 vs the product $O_1 \times O_2$ (Figure 5E). One “best” optimized solution set was selected using TOPSIS for this multi-objective optimization, and is shown in Fig. 5F. In this solution, the second configuration, C_2 is the same as the earlier solution C_2^0 . To satisfy the additional constraint imposed by O_4 , the only stiffness switches between C_1 and C_2 occur in the bottom row of particles. Intuitively, the particles that are most important in determining the forces on the bottom boundary are the particles on the bottom wall. Translating this solution set to experiments, we observe qualitative agreement between simulation and experiment.

4 Conclusions

The heterogeneity of a force network in a granular material is tied to the disordered nature of the constituent contacts. In this work, we showed variability and controllability of the force network using particle stiffness variations, rather than positional changes. Variable stiffness particles were realized by embedding a Field’s metal core in silicone particles. By running a current through a resistive heater co-located with the low-melting-temperature alloy core, we achieved a drop in stiffness ($\sim 2.5\times$) when the particles are heated above the melting temperature of Field’s metal. Although this stiffness change is substantial and has allowed us to qualitatively measure differences in force networks, an optimized particle design could induce a more dramatic particle stiffness ratio and thus more dramatic changes to the force networks in a VS particle packing.

To efficiently sample force networks, we used a discrete element-based simulation that reasonably captures the force law between particles, which we empirically derived. However, the simulator is a simplified model of the physics in the experiment. Our experimental system consistently exhibits a stronger response than what the simulation predicted, which inspires us to build more realistic simulations to understand the relevance of various design parameters in our system. Increased simulation-to-reality matching would improve design outcomes and potentially allow us to discover additional physical mechanisms to control force networks. Finally, although we have only chosen to replicate one solution on the Pareto-Front using the TOPSIS selection criteria, every solution on the Pareto-Front is a valid and optimized solution. In future studies, we will inspect the other solutions on the Pareto Front and evaluate their advantages and shortcomings for different applications.

Finally, our results serve as a proof-of-concept for primitive logic in granular materials. Instilling intelligence in granular materials through stiffness changes allows the material to completely change its response. Although no traditional form of logic has been shown in this system, we believe that the framework presented in this work serves as a universal tool that shows how to optimize a material to perform desirably. Previous works have shown logic capabilities within granular materials⁵⁹, but they

have relied only on the embedded capabilities of the granular material rather than optimizing for a desired response. Similarly, although there have been several numerical studies at making granular logic using this fundamental principle^{60,61}, our results represent a first experimental instantiation. We intend to continue building upon the results herein to realize granular metamaterials that can adapt their property states and force distributions to changing use cases and environments, as well as adapt their logic gates for next-generation mechanical computation.

Author Contributions

S.W.: Methodology, validation, formal analysis, investigation, data curation, writing, review and editing, visualization, and project administration. A.P.: Methodology, formal analysis, validation, writing, and visualization. N.P.: Methodology, investigation, supervision, review and editing. J.Z.: Methodology, formal analysis. A.M.: Methodology. M. D. S.: Investigation, resources. R.K.-B.: Conceptualization, supervision, project administration, review and editing, resources, and funding acquisition. C.S.O.: Conceptualization, supervision, project administration, review and editing, resources, and funding acquisition. J.B.: Conceptualization, supervision, project administration, review and editing, resources, and funding acquisition.

Conflicts of interest

There are no conflicts to declare.

Acknowledgements

This material is based upon work supported by the National Science Foundation under the Designing Materials to Revolutionize and Engineer our Future (DMREF) program (award no. 2118988).

Notes and references

- 1 C. Jiang, F. Rist, H. Wang, J. Wallner and H. Pottmann, *Computer-Aided Design*, 2022, **143**, 103146.
- 2 W. Yang, Z.-M. Li, W. Shi, B.-H. Xie and M.-B. Yang, *Journal of Materials Science*, 2004, **39**, 3269–3279.
- 3 Y. Wang, L. Li, D. Hofmann, J. Andrade and C. Daraio, *Nature*, 2021, **596**, 238–243.
- 4 B. Jenett, C. Cameron, F. Tourlomousis, A. P. Rubio, M. Ochalek and N. Gershenfeld, *Science advances*, 2020, **6**, eabc9943.
- 5 T. Majmudar, M. Sperl, S. Luding and R. P. Behringer, *Physical review letters*, 2007, **98**, 058001.
- 6 E. I. Corwin, H. M. Jaeger and S. R. Nagel, *Nature*, 2005, **435**, 1075–1078.
- 7 E. Brown, N. Rodenberg, J. Amend, A. Mozeika, E. Steltz, M. R. Zakin, H. Lipson and H. M. Jaeger, *Proceedings of the National Academy of Sciences*, 2010, **107**, 18809–18814.
- 8 A. J. Liu and S. R. Nagel, *Soft Matter*, 2010, **6**, 2869–2870.
- 9 A. J. Liu and S. R. Nagel, *Annu. Rev. Condens. Matter Phys.*, 2010, **1**, 347–369.
- 10 D. Bi, J. Zhang, B. Chakraborty and R. P. Behringer, *Nature*, 2011, **480**, 355–358.

- 11 R. P. Behringer and B. Chakraborty, *Reports on Progress in Physics*, 2018, **82**, 012601.
- 12 E. Steltz, A. Mozeika, J. Rembisz, N. Corson and H. Jaeger, *Electroactive Polymer Actuators and Devices (EAPAD) 2010*, 2010, p. 764225.
- 13 Y. Jiang, D. Chen, C. Liu and J. Li, *Soft robotics*, 2019, **6**, 118–132.
- 14 A. Jiang, T. Ranzani, G. Gerboni, L. Lekstutyte, K. Althoefer, P. Dasgupta and T. Nanayakkara, *Soft Robotics*, 2014, **1**, 192–201.
- 15 M. A. Karimi, V. Alizadehyazdi, B.-P. Busque, H. M. Jaeger and M. Spenko, 2020 3rd IEEE International Conference on Soft Robotics (RoboSoft), 2020, pp. 291–296.
- 16 S. G. Fitzgerald, G. W. Delaney and D. Howard, *Actuators*, 2020, p. 104.
- 17 M. Brancadoro, M. Manti, F. Grani, S. Tognarelli, A. Menciacchi and M. Cianchetti, *Frontiers in Robotics and AI*, 2019, **6**, 12.
- 18 M. Brancadoro, M. Manti, S. Tognarelli and M. Cianchetti, *Soft Robotics*, 2020.
- 19 J. D. Brigido-González, S. G. Burrow and B. K. Woods, *Journal of Intelligent Material Systems and Structures*, 2019, **30**, 2581–2594.
- 20 K. Dierichs and A. Menges, *Granular Matter*, 2016, **18**, 25.
- 21 G. Gantzounis, M. Serra-Garcia, K. Homma, J. Mendoza and C. Daraio, *Journal of Applied Physics*, 2013, **114**, 093514.
- 22 A. Leonard, L. Ponson and C. Daraio, *Journal of the Mechanics and Physics of Solids*, 2014, **73**, 103–117.
- 23 L. Bonanomi, G. Theocharis and C. Daraio, *Physical Review E*, 2015, **91**, 033208.
- 24 N. NejadSadeghi, L. Placidi, M. Romeo and A. Misra, *Mechanics Research Communications*, 2019, **95**, 96–103.
- 25 E. Kim and J. Yang, *Functional Composites and Structures*, 2019, **1**, 012002.
- 26 F. Li, P. Anzel, J. Yang, P. G. Kevrekidis and C. Daraio, *Nature communications*, 2014, **5**, 1–6.
- 27 Q. Wu, C. Cui, T. Bertrand, M. D. Shattuck and C. S. O'Hern, *Physical Review E*, 2019, **99**, 062901.
- 28 K. Fu, Z. Zhao and L. Jin, *Advanced Functional Materials*, 2019, **29**, 1901258.
- 29 M. A. Porter, P. G. Kevrekidis and C. Daraio, *Physics Today*, 2015, **68**, year.
- 30 N. NejadSadeghi and A. Misra, *International Journal of Mechanical Sciences*, 2019, **161**, 105042.
- 31 A. Merkel and J. Christensen, *Communications Physics*, 2019, **2**, 1–6.
- 32 A. Parsa, D. Wang, C. S. O'Hern, M. D. Shattuck, R. Kramer-Bottiglio and J. Bongard, *International Conference on the Applications of Evolutionary Computation (Part of EvoStar)*, 2022, pp. 93–109.
- 33 A. Parsa, D. Wang, C. S. O'Hern, M. D. Shattuck, R. Kramer-Bottiglio and J. Bongard, *Proceedings of the Genetic and Evolutionary Computation Conference*, 2022, pp. 122–129.
- 34 A. Parsa, S. Witthaus, N. Pashine, C. O'Hern, R. Kramer-Bottiglio and J. Bongard, *Proceedings of the Genetic and Evolutionary Computation Conference*, 2023, pp. 193–201.
- 35 H. Herrmann, J. Hovi and S. Luding, *Physics of Dry Granular Media*, Springer Netherlands, 2014.
- 36 H. M. Jaeger, S. R. Nagel and R. P. Behringer, *Rev. Mod. Phys.*, 1996, **68**, 1259–1273.
- 37 R. Behringer, D. Howell, L. Kondic, S. Tennakoon and C. Veje, *Physica D: Nonlinear Phenomena*, 1999, **133**, 1–17.
- 38 D. W. Howell, R. P. Behringer and C. T. Veje, *Chaos: An Interdisciplinary Journal of Nonlinear Science*, 1999, **9**, 559–572.
- 39 B. Utter and R. Behringer, *The European physical journal. E, Soft matter*, 2004, **14**, 373–80.
- 40 R. Behringer, H. Jaeger and S. Nagel, *Chaos: An Interdisciplinary Journal of Nonlinear Science*, 1999, **9**, 509–510.
- 41 F. Radjai, M. Jean, J.-J. Moreau and S. Roux, *Phys. Rev. Lett.*, 1996, **77**, 274–277.
- 42 S. Luding, *Phys. Rev. E*, 1997, **55**, 4720–4729.
- 43 J. F. Peters, M. Muthuswamy, J. Wibowo and A. Tordesillas, *Phys. Rev. E*, 2005, **72**, 041307.
- 44 S. F. Edwards and D. V. Grinev, *Granular Matter*, 2003, **4**, 147–153.
- 45 C. S. Campbell, *Powder Technology*, 2006, **162**, 208–229.
- 46 N. Pashine, A. M. Nasab and R. Kramer-Bottiglio, *Soft Matter*, 2023, **19**, 1617–1623.
- 47 W. Shan, T. Lu and C. Majidi, *Smart Materials and Structures*, 2013, **22**, 085005.
- 48 M. J. Puttock and E. G. Thwaite, *Elastic compression of spheres and cylinders at point and line contact*, by M. J. Puttock and E. G. Thwaite, Commonwealth Scientific and Industrial Research Organization Melbourne, 1969, p. 64 p.
- 49 G. D. J. de Jong, in *Étude photo-Élastique d'un empilement de disques*, ed. R. J. Schotting, H. C. J. van Duijn and A. Verruijt, Springer Netherlands, Dordrecht, 2006, pp. 148–161.
- 50 T. Wakabayashi, *Journal of the Physical Society of Japan*, 1950, **5**, 383–385.
- 51 A. Resnick, *Contemporary Physics*, 2016, **58**, 1–1.
- 52 A. Flamant *et al.*, *CR Acad. Sci. Paris*, 1892, **114**, 1465–1468.
- 53 M. Z. Miskin and H. M. Jaeger, *Soft Matter*, 2014, **10**, 3708–3715.
- 54 D. Shah, B. Yang, S. Kriegman, M. Levin, J. Bongard and R. Kramer-Bottiglio, *Advanced Materials*, 2021, **33**, 2002882.
- 55 R. Chiong, T. Weise and Z. Michalewicz, *Variants of evolutionary algorithms for real-world applications*, Springer, 2012, vol. 2.
- 56 M. D. Schmidt and H. Lipson, *Proceedings of the 12th annual conference on Genetic and evolutionary computation*, 2010, pp. 543–544.
- 57 K. Deb, A. Pratap, S. Agarwal and T. Meyarivan, *IEEE transactions on evolutionary computation*, 2002, **6**, 182–197.
- 58 C.-L. Hwang, K. Yoon, C.-L. Hwang and K. Yoon, *Multiple attribute decision making: methods and applications a state-of-the-art survey*, 1981, 58–191.
- 59 F. Li, P. Anzel, J. Yang, P. G. Kevrekidis and C. Daraio, *Nature communications*, 2014, **5**, 5311.
- 60 A. Parsa, D. Wang, C. S. O'Hern, M. D. Shattuck, R. Kramer-

Bottiglio and J. Bongard, Applications of Evolutionary Computation, Cham, 2022, pp. 93–109.

61 Q. Wu, C. Cui, T. Bertrand, M. D. Shattuck and C. S. O'Hern, *Phys. Rev. E*, 2019, **99**, 062901.